CIRCADIAN RHYTHMS

Sex-dimorphic and age-dependent organization of 24-hour gene expression rhythms in humans

Lorenzo Talamanca†, Cédric Gobet†, Felix Naef*

The circadian clock modulates human physiology. However, the organization of tissue-specific gene expression rhythms and how these depend on age and sex is not defined in humans. We combined data from the Genotype-Tissue Expression (GTEx) project with an algorithm that assigns circadian phases to 914 donors, by integrating temporal information from multiple tissues in each individual, to identify messenger RNA (mRNA) rhythms in 46 tissues. Clock transcripts showed conserved timing relationships and tight synchrony across the body. mRNA rhythms varied in breadth, covering global and tissue-specific functions, including metabolic pathways and systemic responses. The clock structure was conserved across sexes and age groups. However, overall gene expression rhythms were highly sex-dimorphic and more sustained in females. Rhythmic programs generally dampened with age across the body.

The circadian clock allows evolutionary adaptation of life to the 24-hour periodicity of Earth's rotation. The clock synchronizes internal body rhythms in behavior and physiology with 24-hour environmental, societal, or feeding cues (*1*–*3*). Perturbations of the clock, such as those caused by sleep disruption and shift work, can lead to pathologies (*4*). Sexual dimorphism exists in gene expression levels across the body (*5*), and many complex phenotypes, including diseases, exhibit sex-dependent characteristics (*6*). However, interactions between sexual dimorphism and molecular circadian rhythms in humans are unexplored (*7*). Likewise, the effects of aging on human physiology are well studied (*8*), but the interplay between circadian oscillations and aging processes is still poorly understood (*9*).

We combined Genotype-Tissue Expression (GTEx) project transcriptomes with an algorithm that assigns circadian times to individuals and tissues (*10*–*12*) to obtain a whole-organism view of 24-hour gene expression rhythms in 46 human tissues. A stratification by sex and age revealed a rich picture of group-specific rhythms, especially in metabolic and cardiovascular tissues, that may provide insights into differential disease incidence rates.

Results

Comprehensive 24-hour gene expression rhythms in 46 human tissues

To study the breadth of rhythmic mRNA programs across the human body, we used data from 16,000 human RNA sequencing (RNA-seq) experiments from 914 donors in the GTEx collection and computed one circadian reference phase for each donor. This phase corresponds to the expected circadian phase in skeletal muscle, hereafter named the donor internal phase (DIP). The algorithm exploits the fact that the circadian phases of tissue samples (typically 10 to 20 per individual) from the same donor are correlated and assumes that relative circadian phases of tissues are conserved across donors. Time of death (TOD) (available from GTEx) may not reflect circadian phase because of the individuals' varying chronotypes (*2*), positions in a time zone, and type of death. In relation to the TOD, clock genes such as *PER2* and *NR1D1* exhibited arrhythmic profiles in most tissues (fig. S1A), and mRNA rhythmicity at the genome-scale was nearly absent (fig. S1B). However, the pairwise correlations between clock transcripts were indicative of a functional clock (fig. S1C). We therefore developed an algorithm to assign DIPs to all donors (Fig. 1A). After correcting for sample covariates to reduce variability that was not due to circadian oscillations (fig. S1D), we applied two steps. For each tissue independently, we used CHIRAL, an algorithm we developed to estimate the tissue internal phases (TIPs) of all samples, which uses a set of seed genes and their assigned weights (fig. S1, E and F). We tested several sets of seed genes and benchmarked CHIRAL using time-labeled human samples from muscle (*13*) (fig. S1G and table S1). We identified a set of 12 genes, consisting of mechanistically well-characterized circadian time-telling transcripts, that performed better than other sets composed of genes showing rhythmicity across mouse tissues. In particular, performance decreases with the set size (fig. S1, H to J) (*14*, *15*). The TIPs from one donor often showed one primary mode, which we assigned as the DIPs (fig. S2, A to D). With the DIPs, we characterized gene expression rhythmicity in 46 tissues by harmonic regression.

DIPs were distributed fairly uniformly along the 24-hour cycle (table S2). TODs and DIPs showed better concordance for fast death compared with slow death (Hardy scale) (fig. S2E). With the DIPs, *PER2* and *NR1D1* showed clear circadian oscillations across all donors (fig. S2F), indicating that the DIPs captured circadian phase more reliably than TODs. Clock transcript oscillations across all tissues showed that although the amplitudes varied, the peak times were aligned, with the tightest being *TEF* and *ARNTL* (*BMAL1*) and the most variable being *NR1D1* (*REVERBA*) (fig. S2G). We used the complex-valued singular value decomposition (cSVD) to summarize the multigene structure of clocks across multiple conditions. The first mode, which captured >95% of the variance, showed that the human clock module comprises two main groups of antiphasic genes, plus fewer genes with a phase angle (Fig. 1B). Clocks across tissues were well synchronized, showing relative offsets of only a few hours; the adrenal gland had the earliest phase, perhaps related to the distinct role of adrenal glucocorticoids in systemic clock organization (*16*). Metabolic tissues (adipose tissue, esophagus, cardiovascular tissues) showed the highest amplitudes, whereas brain tissues and testis had the lowest (Fig. 1B) (*17*), as reflected by the clock genes *PER3* and *ARNTL* (Fig. 1C).

To test whether the DIPs also unveil mRNA rhythms associated with systemic signals, we considered heat shock response genes, which exhibit rhythmic activity in mice (*18*). Heat shock genes (HSF1 targets) showed clear diurnal expression patterns; the highest oscillatory amplitude was observed in brain tissues, which peaked between 8 and 10 p.m., near the time of highest body temperature in humans (*19*) (Fig. 1D). Compared with the clock, we observed a larger spread in peak phases across tissues; the peak times of both *HSPH1* and *HSPA1B* were almost antiphasic in spleen and amygdala (Fig. 1E). The high-amplitude heat shock program in many brain regions may reflect a pressure for high proteome integrity in nonrenewing tissues (*20*).

Genome-wide 24-hour rhythmicity (fig. S3A and tables S3 and S4) across tissues showed morning (centered on 7 a.m.) and evening (7 p.m.) waves of gene expression throughout the body (Fig. 1, F and G), with metabolic tissues showing the most rhythmicity and brain tissues the least, a property that was stable across the different seed gene sets (*15*, *21*) (fig. S3B). These waves showed slight temporal shifts that followed the phases of the core clock (Fig. 1B): Several glands showed early phases, followed by cardiovascular, metabolic, and brain tissues (Fig. 1G). Depending on the tissue, we found between tens and several hundreds of rhythmic transcripts with peak-to-trough ratios greater than 2 (Fig. 1H). Besides clock genes, more than 100 transcripts were rhythmic in at least 20 tissues, including known rhythmic genes such as *NFIL3* and *PDK4* as

Institute of Bioengineering, School of Life Sciences, Ecole Polytechnique Fédérale de Lausanne (EPFL), CH-1015 Lausanne, Switzerland.
*Corresponding author. Email: felix.naef@epfl.ch
†These authors contributed equally to this work.

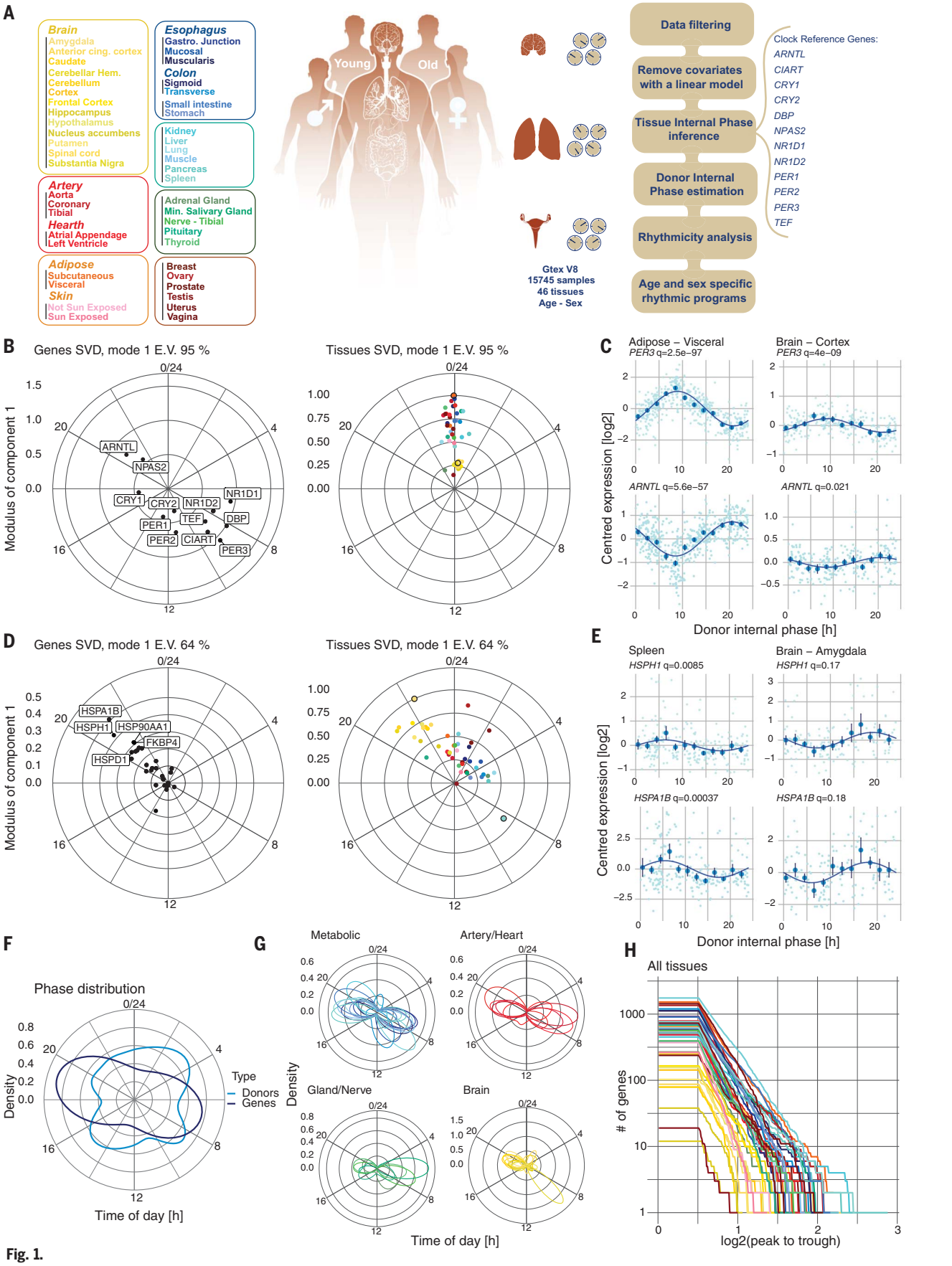
A
Brain
Amygdala
Anterior cing. cortex
Caudate
Cerebellar Hem.
Cerebellum
Cortex
Frontal Cortex
Hippocampus
Hypothalamus
Nucleus accumbens
Putamen
Spinal cord
Substantia Nigra
Artery
Aorta
Coronary
Tibial
Hearth
Atrial Appendage
Left Ventricle
Adipose
Subcutaneous
Visceral
Skin
Not Sun Exposed
Sun Exposed
Esophagus
Gastro. Junction
Mucosal
Muscularis
Colon
Sigmoid
Transverse
Small intestine
Stomach
Kidney
Liver
Lung
Muscle
Pancreas
Spleen
Adrenal Gland
Min. Salivary Gland
Nerve - Tibial
Pituitary
Thyroid
Breast
Ovary
Prostate
Testis
Uterus
Vagina
Young
Old
Gtex V8
15745 samples
46 tissues
Age - Sex
Data filtering
Remove covariates with a linear model
Tissue Internal Phase inference
Donor Internal Phase estimation
Rhythmicity analysis
Age and sex specific rhythmic programs
Clock Reference Genes:
ARNTL
CIART
CRY1
CRY2
DBP
NPAS2
NR1D1
NR1D2
PER1
PER2
PER3
TEF
B
Genes SVD, mode 1 E.V. 95 %
Tissues SVD, mode 1 E.V. 95 %
Modulus of component 1
ARNTL
NPAS2
CRY1
CRY2
NR1D2
NR1D1
TEF
DBP
PER1
PER2
CIART
PER3
C
Adipose – Visceral
PER3 q=2.5e−97
Brain – Cortex
PER3 q=4e−09
ARNTL q=5.6e−57
ARNTL q=0.021
Centred expression [log2]
Donor internal phase [h]
D
Genes SVD, mode 1 E.V. 64 %
Tissues SVD, mode 1 E.V. 64 %
Modulus of component 1
HSPA1B
HSPH1
HSP90AA1
FKBP4
HSPD1
E
Spleen
HSPH1 q=0.0085
Brain – Amygdala
HSPH1 q=0.17
HSPA1B q=0.00037
HSPA1B q=0.18
Centred expression [log2]
Donor internal phase [h]
F
Phase distribution
Density
Type
Donors
Genes
Time of day [h]
G
Metabolic
Artery/Heart
Gland/Nerve
Brain
Density
Time of day [h]
H
All tissues
# of genes
log2(peak to trough)

Fig. 1.

Fig. 1. Global circadian ordering of GTEx project data identifies synchronous circadian clocks in 46 human tissues. (**A**) Algorithm to assign one donor internal phase (DIP) to 914 individuals in the GTEx v8 RNA-seq dataset. The list of all tissues studied and the color scheme used in the figures are shown on the left. Anterior cing. cortex, anterior cingulate cortex; cerebellar hem., cerebellar hemisphere; gastro. junction, gastrointestinal junction; min. salivary gland, minor salivary gland. (**B**) First gene (left) and tissue (right) complex (eigen-)vectors from the cSVD performed on clock reference genes (first module explains 95% of the 24-hour variance; E.V., explained variance). In the polar plots, phases have been converted to 24-hour time, and time runs clockwise. (**C**) mRNA expression levels (log_2, centered) of two clock genes (*PER3* and *ARNTL*) in two representative tissues. Mean and standard error (SE) were computed in 2-hour bins, and harmonic regression fits are shown (dark blue). Benjamini-Hochberg (BH) adjusted *p* values [*q*(BH)] are reported. (**D**) Heat shock gene module (top 20 HSF1 targets), displayed as in (B). (**E**) mRNA expression levels (log_2, centered) for two heat shock response genes (*HSPH1* and *HSPA1B*), represented as in (C). (**F**) Polar density plot of the DIPs and of the peak times of rhythmic genes. (**G**) Phase densities of rhythmic genes [*q*(BH) < 0.2 and log_2 peak-trough > 0.5] for various groups of tissues. (**H**) Number of rhythmic genes [*q*(BH) < 0.2 and log_2 peak-trough > 0.5], with peak-trough amplitude higher than a threshold (*x* axis, log_2) plotted as a function of the threshold across 46 tissues.

well as glucocorticoid-responsive genes such as *FKBP5* and the proinflammatory cytokine receptors interleukin 1 receptor–like 1 and 2 (*IL1RL1*, *IL1R2*) (table S5). Twelve-hour ultradian mRNA rhythms were detected in several tissues, notably in ovary and liver (fig. S3C).

To characterize regulatory mechanisms, we used cSVD to integrate transcription factor (TF) targets. Putative regulators of both the morning and evening waves were involved in immunity, core clock, carbohydrate metabolism, and cell proliferation (fig. S3D and table S5). Among TFs that explained the most variance were the core clock dimer CLOCK:BMAL1 (peak target accumulation at 10 a.m.) and glucocorticoid receptor (GR) NR3C1 (5 p.m.) that corresponded to GR-repressed genes (*22*). In the evening, MYC and MYCN (7 p.m., cell proliferation), X-box-binding protein 1 (XBP1) (8 p.m., response to unfolded protein response), and peroxisome proliferator–activated receptor gamma coactivator 1 (PPARGC1) (8 p.m., energy metabolism) were activated. During the night, IRF2 (2 a.m., interferon regulatory factor) and STAT2 (3 a.m., cytokine response) activities peaked. Similar TFs showed rhythmic activities in mouse liver (*23*). Enriched gene functions showed coherence across many tissues (fig. S4A and table S5). Starting at midnight, immune response genes peaked early during the night, consistent with the above IRF2 and STAT2 TFs, followed by a response to cholesterol in the early day that coincided with peak times of serum cholesterol levels (*24*). Around 9 a.m., we observed a peak for caffeine response, followed by energy homeostasis, gluconeogenesis, and lipid metabolism genes. mRNAs involved in amino acid and glucose metabolism, as well as protein synthesis and folding, peaked in the early afternoon, which extended into the evening. Cell-cycle pathways peaked in the evening to late night, which coincided with the predicted MYC and MYCN activities. Therefore, pan-rhythmic gene functions in humans largely consist of timed metabolic processes that reflect a switch between low- and high-energy states during the rest-activity cycle. Among functions that showed tissue specificity, lipid metabolism was particularly rhythmic in the liver, as was amino acid metabolism in the intestine and heat shock response across the brain tissues (fig. S4B).

Human sexual dimorphism in circadian rhythms

We leveraged DIPs to analyze sex-dimorphic mRNA rhythms. The relative phases and amplitudes of clock genes were conserved in males and females (Fig. 2A), and the distributions of DIPs were similar for males and females (Fig. 2B). To analyze sex-dimorphic clock output programs, we used a model selection approach to classify each transcript into five statistical scenarios (models) depending on the rhythmic behavior in both sexes (*25*). The number of rhythmic genes was higher in females by about twofold at all amplitude thresholds (Fig. 2C and fig. S5). Although tissues such as esophagus, skeletal muscle, and adipose tissue did not differ much, the stratification by sex unveiled several highly dimorphic tissues (Fig. 2D). Notably, females had considerably more rhythmic transcripts in the adrenal gland and liver (Fig. 2D).

Cardiovascular tissues are known sites of circadian regulation (*26*) that exhibit circadian rhythmicity in data from the GTEx project (*12*). In the heart (atrial appendage), the total number of rhythmic genes and their peak phases were similar in males and females (Fig. 2, E and F). However, only about 50% of rhythmic genes were shared between male and female, with the remaining rhythms either being specific to one sex or showing different rhythmic patterns (Fig. 2G).

Liver exhibits marked circadian physiology and sex-dependent gene expression in humans (*5*). We found a strong enrichment of mRNA rhythms in females at all amplitudes, mostly as an extensive morning wave (Fig. 2, H to J). Three pathways, with sex-dependent mRNA rhythms in mice (*27*), showed enriched rhythmicity in female livers: xenobiotic detoxification, fatty acid oxidation, and cholesterol synthesis (fig. S6A). In the latter, nearly all enzymes, including the rate-limiting and statin target 3-hydroxy-3-methylglutaryl-CoA reductase (HMGCR), showed rhythmicity in females that was damped or absent in males (fig. S6C). In detoxification, many phase I and II enzymes were strongly enriched in female-specific cyclers (Fig. 2L) (*28*). Female-specific rhythms in the liver were predicted to be driven by heat shock transcription factor 1 (HSF1) and peroxisome proliferator–activated receptor gamma (PPARG) (fig. S6A).

The adrenal gland also exhibited more rhythmic mRNAs in females than in males, centered at midday (Fig. 2K). Among those, GR targets were enriched, which could reflect autocrine signaling (fig. S6B). Because glucocorticoid signaling is a systemic synchronizer and organizer of peripheral rhythms (*16*), this might corroborate with the overall increased rhythmicity in females at transcriptional and physiological levels (*7*).

Age-dependent circadian reprogramming of human gene expression

We analyzed how aging reprograms daily rhythmic gene expression across the human body. Donors were divided into two age groups: less than 50 years of age (38 ± 9 years) and more than 60 years of age (65 ± 3 years). The overall amplitudes, phases, and relative relationships of the clock genes were conserved with age (Fig. 3A). Rhythmic transcripts showed two waves in both age groups (Fig. 3B) but were overall strongly damped in the older donors (Fig. 3C and fig. S7) (*29*). The latter showed one-third of rhythmic genes with peak-to-trough ratios greater than 4 (Fig. 3C); such loss of rhythmicity with aging occurred in most but not all tissues (Fig. 3D). For instance, adipose tissues, esophagus, and skeletal muscle showed conserved rhythmicity across age, with most genes exhibiting statistically identical rhythms in the two groups (model 4, colored mustard, in Fig. 3D). This is illustrated in subcutaneous adipose tissue, where the morning and evening waves are pronounced in both younger and older donors (Fig. 3E), with a majority of shared (model 4) mRNA rhythms (Fig. 3, F and G).

We next focused on the coronary arteries, a tissue that strongly lost rhythms with age. Although morning and evening transcript waves were observed in both groups (Fig. 3H), the number of rhythmic mRNAs in older donors was about half that in younger donors, across all amplitudes (Fig. 3, I and J). Programs that lost rhythmicity include cholesterol biosynthesis, fatty acid synthesis, and the regulation of glycolysis (Fig. 3L and fig. S8A), which are processes known to be deregulated in vascular smooth muscle cells in cardiovascular diseases (*30*). Most enzymes in the cholesterol biosynthesis pathway, including *HMGCR*, were rhythmically expressed in young coronary arteries but lost this feature with age (Fig. 3L).

Comparing the ovaries of pre- and postmenopausal women revealed that both lost

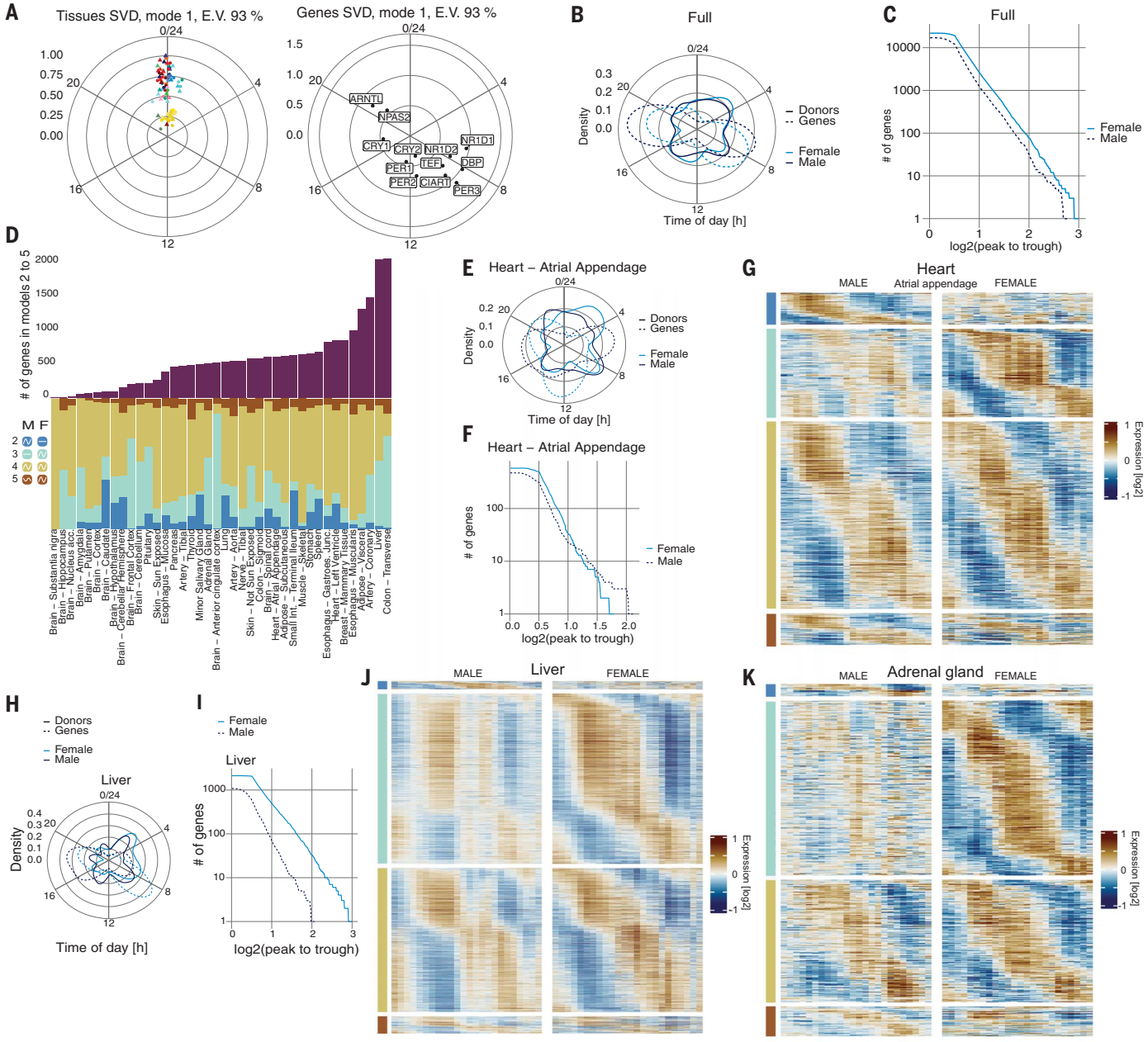

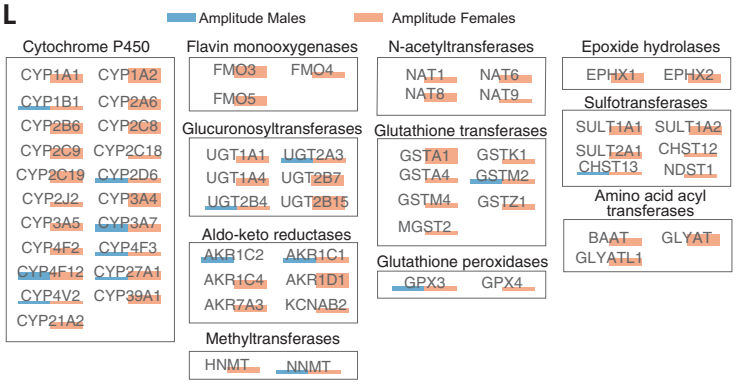

Fig. 2. Human sexual dimorphism in circadian mRNA rhythms. (**A**) First gene (left) and tissue (right) vectors of cSVD performed on clock reference genes for males (triangle) and females (circle). The first module explains 93% of the 24-hour variance (E.V.). (**B**) Polar densities of DIPs (solid line) and gene peak phases (dashed line) in males (dark blue) and females (light blue). (**C**) Number of 24-hour rhythmic genes with an amplitude higher than a threshold as a function of the threshold in all tissues combined. (**D**) Summary of total number of rhythmic genes in each tissue (top) divided according to four statistical models (bottom): model 2 (blue), model 3 (cyan), model 4 (mustard), and model 5 (brick). M, male; F, female. (**E**) Heart atrial appendage represented as in (B). (**F**) Heart atrial appendage illustrated as in (C). (**G**) Heart atrial appendage: Heatmap of mRNA levels for genes in models 2 to 5 illustrates model selection. Log_2 (mean centered) expression of all samples in the two categories, low (blue) to high (brown), represented by 1-hour bins plotted with a 4-hour window moving average. (**H**) Liver tissue summarized as in (E). (**I**) Liver as in (F). (**J**) Liver as in (G). (**K**) Adrenal gland as in (G). (**L**) Liver: Visualization of rhythmic genes in the biotransformation meta pathway (WP702) colored according to amplitude of genes in males (blue) and females (red). All genes shown satisfy q(BH) < 0.2 and peak-trough > 0.5 (log_2) in one or both sexes (see methods).

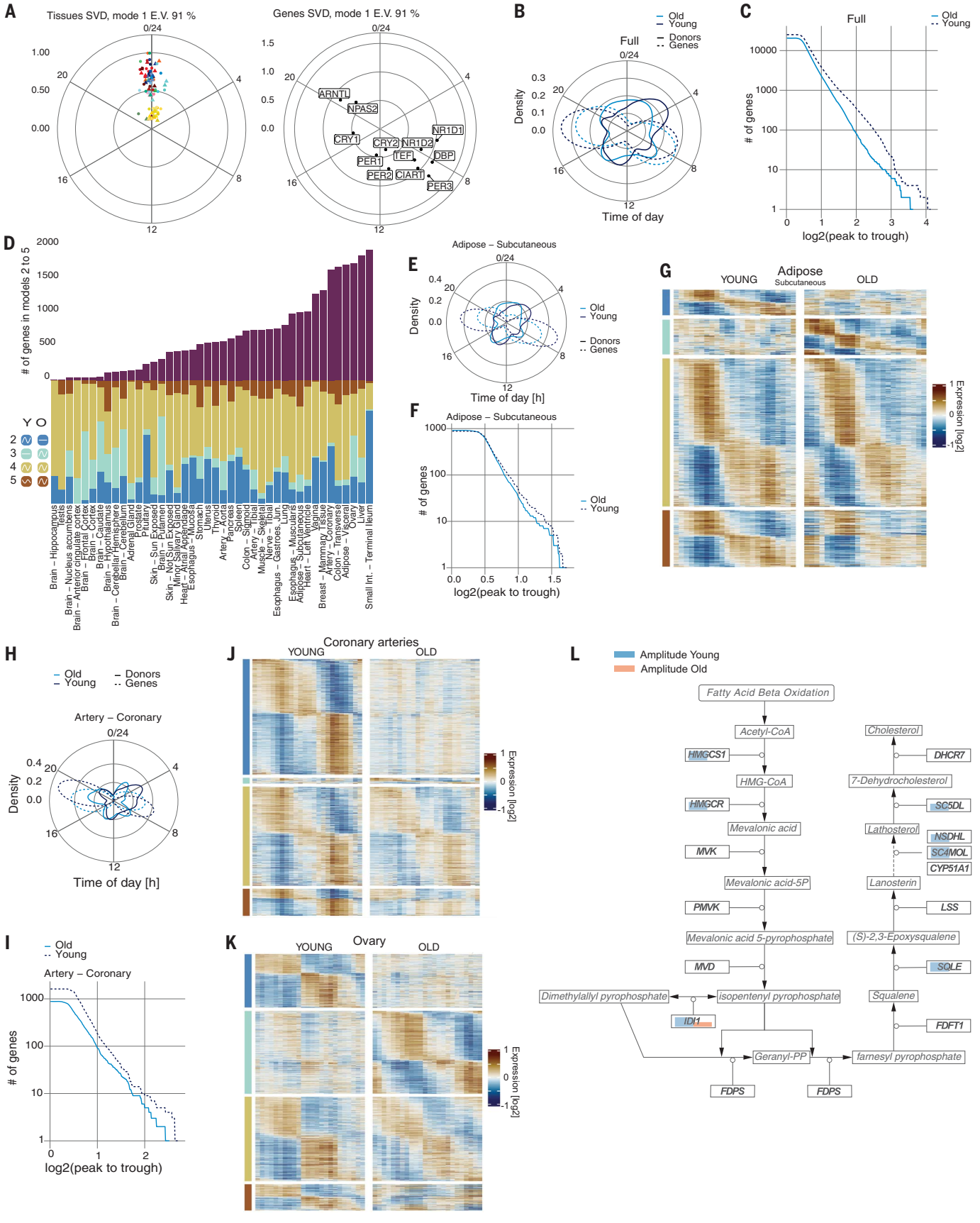

Fig. 3. Age-dependent circadian reprogramming of human gene expression. (**A**) First gene (left) and tissue (right) vectors of cSVD performed on CRGs for younger (triangles) and older (circles) donors. The first module explains 91% of the 24-hour variance (E.V.). (**B**) Polar densities of the DIPs (solid line) and

gene phase (dashed line). (**C**) Number of 24-hour-rhythmic genes with an amplitude higher than a threshold as a function of the threshold in all tissues combined for younger (dark blue) and older (light blue) donors. (**D**) Summary of the number of rhythmic genes in each tissue divided according to the model selection approach [model 2 (blue), model 3 (cyan), model 4 (mustard), and model 5 (brick)]. Y, younger; O, older. (**E**) Adipose subcutaneous tissue represented as in (C). (**F**) Adipose subcutaneous tissue illustrated as in (B). (**G**) Adipose subcutaneous tissue: Heatmap of genes in models 2 to 5. Log_2 (mean-centered) expression of all samples in the two categories, low (blue) to high (brown), represented by 1-hour bins plotted with a 4-hour window moving average. (**H**) Coronary artery: Polar density plot of DIPs (solid line) and peak phase of rhythmic genes (dashed line) for young (dark blue) and old (light blue). (**I**) Coronary artery: Number of genes with an amplitude higher than a threshold as a function of the threshold for young (dark blue) and old (light blue). (**J**) Coronary arteries as in (G). (**K**) Ovary as in (G). (**L**) Coronary artery: Visualization of cholesterol biosynthesis pathway (WP197) colored according to amplitude of genes in young (blue) and old (light red). All genes shown satisfy $q(BH) < 0.2$ and peak-trough > 0.5 (log_2) in one or both age groups (see methods).

and gained mRNA rhythms (Fig. 3K). Although rhythmicity in lipid and cholesterol biosynthesis was suppressed in older donors, as in the coronary arteries (fig. S8B), stress, and in particular heat shock response genes, became rhythmic, as supported by predicted HSF1 TF activity (fig. S8, B and C). This signature of a thermal stress response in postmenopausal women may reflect circadian patterns of temperature control (*31*).

In some tissues, genes switched from a 24-hour to a 12-hour ultradian periodicity with age. In the pituitary gland, liver, and colon, 12-hour rhythms arose in 30 to 50% of genes classified as only rhythmic in young donors (fig. S8, D and F). In humans, these tissues regulate rhythms of temperature, energy metabolism, and absorption. Such destabilization of 24-hour periodicity in favor of an ultradian state as a result of aging might reflect differences in the reception of external cues in older individuals (*32*).

Discussion

We developed an algorithm to temporally order GTEx samples that could overcome several limitations of postmortem data through preprocessing, controlled statistics, and formulation in terms of a population-level phase model (DIP). Nevertheless, sensitivity to data quality, seed gene sets, complex covariate structures, or sampling bias cannot be fully ruled out, and the dataset is underpowered to comprehensively study the cross-interaction of sex and age. Clocks were largely in-phase in 46 analyzed tissues, with the adrenal gland peaking earliest. The concomitant signature of a sizable wave of negative GR targets in the afternoon suggests that released adrenal glucocorticoids play a crucial role in human body-wide circadian synchronization, including overall increased rhythmicity in females. HSF1 targets contributed a considerable portion of the body's 24-hour rhythms and showed sex and age dependency. The observation that rhythmic liver transcript levels, particularly in xenobiotic detoxification, were prevalent in females may reflect a sex-dimorphic incidence of liver diseases (*33*). Similarly, the loss of mRNA rhythms with age in coronary arteries correlates with age-dependent incidence rates of cardiovascular diseases (*34*). The identified differences in 24-hour rhythmic processes across sexes and ages may help improve patient-specific chronopharmacology (*35*).

REFERENCES AND NOTES

1. J. Aschoff, *Science* **148**, 1427–1432 (1965).
2. T. Roenneberg *et al*., *Sleep Med. Rev.* **11**, 429–438 (2007).
3. C. Dibner, U. Schibler, U. Albrecht, *Annu. Rev. Physiol.* **72**, 517–549 (2010).
4. C. R. Cederroth *et al*., *Cell Metab.* **30**, 238–250 (2019).
5. M. Oliva *et al*., *Science* **369**, eaba3066 (2020).
6. C. Ober, D. A. Loisel, Y. Gilad, *Nat. Rev. Genet.* **9**, 911–922 (2008).
7. S. T. Anderson, G. A. FitzGerald, *Science* **369**, 1164–1165 (2020).
8. R. Yamamoto *et al*., *Nat. Commun.* **13**, 5803 (2022).
9. V. A. Acosta-Rodríguez, F. Rijo-Ferreira, C. B. Green, J. S. Takahashi, *Nat. Commun.* **12**, 2862 (2021).
10. H. R. Ueda *et al*., *Proc. Natl. Acad. Sci. U.S.A.* **101**, 11227–11232 (2004).
11. R. C. Anafi, L. J. Francey, J. B. Hogenesch, J. Kim, *Proc. Natl. Acad. Sci. U.S.A.* **114**, 5312–5317 (2017).
12. M. D. Ruben *et al*., *Sci. Transl. Med.* **10**, eaat8806 (2018).
13. L. Perrin *et al*., *eLife* **7**, e34114 (2018).
14. J. Yeung *et al*., *Genome Res.* **28**, 182–191 (2018).
15. R. Zhang, N. F. Lahens, H. I. Ballance, M. E. Hughes, J. B. Hogenesch, *Proc. Natl. Acad. Sci. U.S.A.* **111**, 16219–16224 (2014).
16. P. Pezük, J. A. Mohawk, L. A. Wang, M. Menaker, *Endocrinology* **153**, 4775–4783 (2012).
17. D. Morse, N. Cermakian, S. Brancorsini, M. Parvinen, P. Sassone-Corsi, *Mol. Endocrinol.* **17**, 141–151 (2003).
18. H. Reinke *et al*., *Genes Dev.* **22**, 331–345 (2008).
19. J. Aschoff, *J. Therm. Biol.* **8**, 143–147 (1983).
20. R. San Gil, L. Ooi, J. J. Yerbury, H. Ecroyd, *Mol. Neurodegener.* **12**, 65 (2017).
21. L. S. Mure *et al*., *Science* **359**, eaao0318 (2018).
22. H. M. Reichardt *et al*., *EMBO J.* **20**, 7168–7173 (2001).
23. J. Wang *et al*., *Cell Metab.* **25**, 102–117 (2017).
24. P. J. Jones, D. A. Schoeller, *J. Lipid Res.* **31**, 667–673 (1990).
25. B. D. Weger *et al*., *Proc. Natl. Acad. Sci. U.S.A.* **118**, e2015803118 (2021).
26. S. C. McLoughlin, P. Haines, G. A. FitzGerald, in *Circadian Rhythms and Biological Clocks, Part B*, A. Sehgal, Ed., vol. 552 of *Methods in Enzymology* (Elsevier, 2015), pp. 211–228.
27. B. D. Weger *et al*., *Cell Metab.* **29**, 362–382.e8 (2019).
28. Y.-F. Lu *et al*., *Chronobiol. Int.* **30**, 1135–1143 (2013).
29. C.-Y. Chen *et al*., *Proc. Natl. Acad. Sci. U.S.A.* **113**, 206–211 (2016).
30. J. Shi, Y. Yang, A. Cheng, G. Xu, F. He, *Am. J. Physiol. Heart Circ. Physiol.* **319**, H613–H631 (2020).
31. R. R. Freedman, D. Norton, S. Woodward, G. Cornélissen, *J. Clin. Endocrinol. Metab.* **80**, 2354–2358 (1995).
32. D. Weinert, *Chronobiol. Int.* **17**, 261–283 (2000).
33. S. Bellentani, F. Scaglioni, M. Marino, G. Bedogni, *Dig. Dis.* **28**, 155–161 (2010).
34. P. Jousilahti, E. Vartiainen, J. Tuomilehto, P. Puska, *Circulation* **99**, 1165–1172 (1999).
35. J. Bicker, G. Alves, A. Falcão, A. Fortuna, *Br. J. Pharmacol.* **177**, 2215–2239 (2020).
36. L. Talamanca, C. Gobet, F. Naef, Sex-dimorphic and age-dependent organization of 24-hour gene expression rhythms in human, Zenodo (2022); https://doi.org/10.5281/zenodo.7199055.

ACKNOWLEDGMENTS

The GTEx project was supported by the Common Fund of the Office of the Director of the National Institutes of Health and by the National Cancer Institute (NCI); National Human Genome Research Institute (NHGRI); National Heart, Lung, and Blood Institute (NHLBI); National Institute on Drug Abuse (NIDA); National Institute of Mental Health (NIMH); and National Institute of Neurological Disorders and Stroke (NINDS). The data used in this manuscript were obtained from the GTEx Portal on 12 April 2020 and dbGaP accession number phs000424.GTEx.v8.p2.c1.GRU on 30 March 2022. We thank F. Gachon and P. De Los Rios for insightful discussions. **Funding:** This project was funded by a Swiss National Science Foundation individual project grant 310030B_201267 to F.N. **Author contributions:** Conceptualization: L.T., C.G., F.N.; Formal analysis: L.T., C.G.; Funding acquisition: F.N.; Methodology: L.T., C.G., F.N.; Investigation: L.T., C.G., F.N.; Software: L.T., C.G.; Supervision: F.N.; Writing – original draft: L.T., C.G., F.N.; Writing – review and editing: L.T., C.G., F.N. **Data and materials availability:** GTEx V8 (dbGaP Accession phs000424.v8.p2) is publicly available at https://www.gtexportal.org/home/datasets, and complete metadata can be requested from dbGaP. Table S3 is available at Zenodo (*36*). Code is available at https://github.com/naef-lab/CHIRAL. **Competing interests:** The authors declare that they have no competing interests. **License information:** Copyright © 2023 the authors, some rights reserved; exclusive licensee American Association for the Advancement of Science. No claim to original US government works. https://www.science.org/about/science-licenses-journal-article-reuse

SUPPLEMENTARY MATERIALS

science.org/doi/10.1126/science.add0846
Materials and Methods
Figs. S1 to S4
Tables S1 to S5
References (*37*–*49*)
MDAR Reproducibility Checklist
Appendix A

View/request a protocol for this paper from *Bio-protocol*.

Submitted 13 June 2022; accepted 5 January 2023
10.1126/science.add0846